

Atomic nanofabrication with complex light fields

M. MÜTZEL¹
U. RASBACH¹
D. MESCHEDÉ^{1,✉}
C. BURSTEDDE²
J. BRAUN²
A. KUNOTH²
K. PEITHMANN³
K. BUSE³

¹ Institut für Angewandte Physik, Universität Bonn, Wegelerstr. 8, 53115 Bonn, Germany
² Institut für Angewandte Mathematik, Universität Bonn, Wegelerstr. 6, 53115 Bonn, Germany
³ Physikalisches Institut, Universität Bonn, Wegelerstr. 8, 53115 Bonn, Germany

Received: 21 March 2003/Revised version: 22 May 2003
Published online: 8 August 2003 • © Springer-Verlag 2003

ABSTRACT The method of neutral atom lithography allows one to transfer to a substrate a 2D intensity modulation of an atomic beam imposed by an inhomogeneous light field. The complexity of the pattern depends on the properties of the light field constructed from the superposition of multiple laser beams. For the design of suitable light fields we present a mathematical model with a corresponding numerical simulation of the so-called inverse problem. Furthermore, details of an experiment carried out with a holographically reconstructed light field are discussed.

PACS 02.60.Pn; 42.40.My; 42.40.Pa; 42.50.Vk

1 Introduction

Laser cooling [1] and atom optics [2] have opened the door to manipulating atomic motion at the nanometer scale. In atomic nanofabrication (ANF) [3] optical dipole forces are used to steer an atomic beam into a pattern with sub-micrometer resolution. In this method, the inhomogeneous intensity distribution of the light field acts as an immaterial light mask. On impact, the atoms are either accumulated to directly grow a 2D structure (so-called direct deposition, or DD), or they modify a resist-covered surface (so-called neutral atom lithography, or NAL), which is then prepared by chemical processing steps. In the first experiments by Timp et al. [4] and McClelland et al. [5], simple but extended and precise arrays of lines were formed in a single-step DD process. The pattern represented a one-to-one image of the laser interference pattern created immediately above the surface.

In order to create more sophisticated 2D structures several light beams were superposed with beam-splitters and mirrors [6, 7]. This arrangement, however, rapidly becomes clumsy if more than two or three light beams are required. A beautiful atom holographic fabrication method for complex structures has been demonstrated by the group of Shimizu employing both amplitude [8] and phase [9] masks. However, it requires the application of atomic matter waves, which to this day exist with very low intensities, causing extremely long exposure times.

We have prepared and applied a holographic element that is capable of simultaneously diffracting an incoming laser beam into multiple beams that may be very narrowly spaced [10]. Figure 1 shows the resulting atom pattern produced with a thermal atomic beam that was transversely laser cooled. In principle this technique allows any interference pattern that is consistent with Maxwell's equations to be generated. Since volume holograms are used, any diffraction angle up to $\pm 90^\circ$ with respect to the surface normal of the crystal is possible. This covers 180° . Thus by using two (or even more) crystals that are facing each other on both sides of the interference region, it will be possible to generate diffracted beams of any direction.

One essential aspect of image formation is the patterning contrast. Here we use a transfer function approach to obtain a simple estimate of contrast to be expected by 1D and 2D focussing of atoms with light masks. Next, a mathematical model is introduced for the design of light fields generating the nanoscale light mask. Based on this model, numerical forward calculations indicate what types of light intensity patterns are to be expected, if the directions of the beams and their amplitudes are known. We further investigate the solution of the inverse problem which serves as a basis for numerical backward simulations. Here the task is to (approximately) reconstruct from a given pattern the required directions and intensities, which are correlated to their expansion coefficients, of the laser beams. In this paper we specialize to a fixed set of beam directions. From a mathematical point of view, the definition of a 'good' (approximate) reconstruction is not

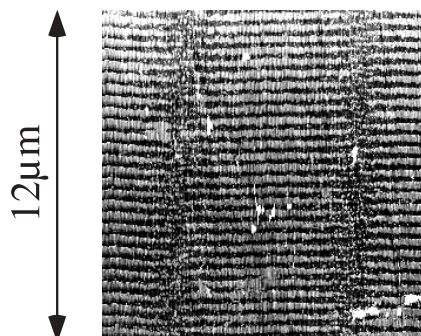


FIGURE 1 Atomic nanofabrication with neutral atom lithography (from [10])

clear beforehand. Finally, we give a detailed analysis of an experimental realization of this method reported in [10].

2 Atomic focussing by 1D and 2D light fields

The atom-optical properties of light fields acting on atomic motion through dipole forces have been studied theoretically [11, 12] and have also received detailed experimental analysis [13]. They fundamentally rely on the force acting on the atoms travelling in an inhomogeneous light field with intensity distribution $I(x) = I_{\max} f(x)$, where $f(x)$ describes the normalized spatial variation of the light field:

$$\mathbf{F}(x) = -\nabla U(x) = -\frac{\hbar\gamma^2}{8\Delta I_{\text{sat}}}\nabla I(x) \equiv U_{\max}\nabla f(x). \quad (1)$$

$U(x)$ is the potential energy for an atom with a resonance frequency detuned by Δ from the light mask frequency. $I_{\text{sat}} \equiv \pi\hbar c/3\lambda^3\tau$ is the saturation intensity of the atomic transition with wavelength λ , c is the speed of light, and h is Planck's constant. The atomic excited state lifetime is τ .

Trajectory simulations analogous to those in Fig. 2 are frequently used to describe the atom-optical focussing properties of standing wave light fields on atoms. For this purpose the inhomogeneous light field (Fig. 3a) is treated as an array of microlenses. Deviations from the central narrow feature caused by the optical lens are interpreted in terms of spherical and other aberrations.

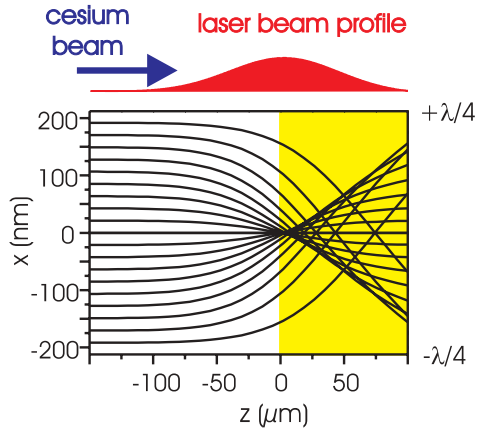


FIGURE 2 Numerically calculated trajectories in a 1D standing wave. The maximum of the transverse Gaussian laser beam profile is at the surface of the substrate at $z = 0$

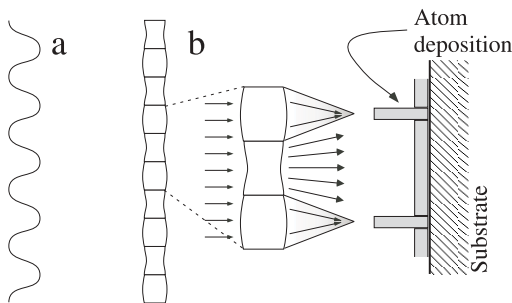


FIGURE 3 A 1D standing wave (a) can be treated as a 1D array (with $\lambda/2$ -unit cell) of a periodic system of focussing and defocussing lenses (b). The defocussing lenses very naturally explain the generation of the pedestal observed when light masks are used

Let us take instead a complementary approach that gives a novel and more intuitive view of image distortion. For this purpose we use the transfer function $x_{\text{foc}} = x_{\text{foc}}(x)$ describing the position x_{foc} in the focal plane for an atom entering the standing wave at position x (see Fig. 4a). A useful empirical approximation is actually given by $x_{\text{foc}} = 2x^5/(1+x^4)$, where x is measured in units of $\lambda/4$.

The zero slope of $x_{\text{foc}}(x)$ near $x = 0$ indicates the focal spot that is the most prominent and usually very narrow feature of this method. Atoms entering the field near the antinodes, $x = \pm\lambda/4$, however, are defocussed. In this region the transfer function is well approximated by $x_{\text{foc}} = 2(x \pm \lambda/4)$. The linear relation indicates an even distribution of these atoms extending in this case uniformly throughout the $\lambda/2$ unit cell, and resulting in a constant pedestal and fundamentally limiting the number of atoms concentrated in the focus. It is this defect that is elsewhere referred to as ‘‘spherical aberration’’.

A measure of the contrast C may be defined by $C = H/(H+B)$, where H and B are the heights of the central peak (with width W) and the pedestal, respectively (see Fig. 5). In a simplified model let us assume that the pedestal is dominated by spherical aberrations (i.e. defocussing in our model) while velocity and beam spread contribute to the width of the central peak only. Typical contrast values can then be

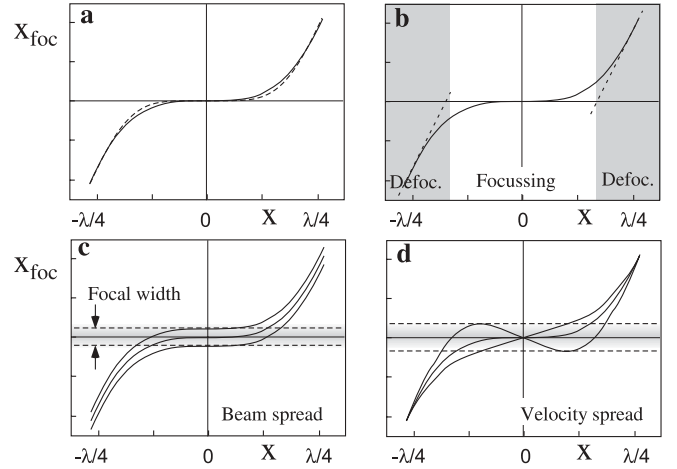
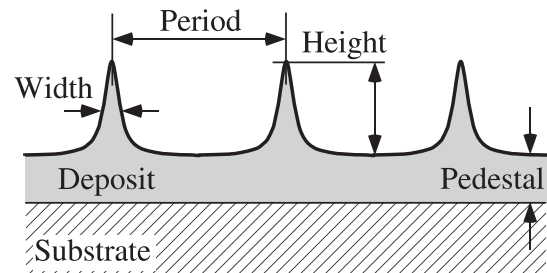


FIGURE 4 Focussing by a 1D standing wave light field; x_{foc} : trajectory coordinate in the focal plane vs. input coordinate x . **a** x_{foc} for a perfectly collimated beam. The dashed line is $2x^5/(1+x^4)$. **b** Focussing and defocussing regions. **c** Influence of beam spread. **d** Influence of velocity spread



$$\text{Contrast} = \text{Height}/(\text{Height}+\text{Pedestal})$$

$$C = H/(H+B)$$

FIGURE 5 Definition of parameters for atomic nanofabrication

inferred from the observation that 1/2 of the accumulated flux of atoms F entering the 1D unit cell of length $\lambda/2$ are evenly redistributed to form the pedestal, and hence $B = F/\lambda$, while the other half is focussed to a height $H = F/2W$. Consequently we find for the 1D case $C_{1D} = \lambda/(\lambda + 2W)$. It is straightforward to extend this analysis to the 2D case for point-like focussing. Now 3/4 of the atoms are redistributed within $(\lambda/2)^2$, leading to $B_{2D} = 3F/\lambda^2$, and 1/4 is focussed within the height $H_{2D} = F/(2W)^2$, resulting in an estimated contrast $C_{2D} = \lambda^2/[\lambda^2 + 3(2W)^2]$. Any complex pattern will consist of a mixture of point-like and line-like structures, and with a moderate requirement that the focussing is better than $W \leq \lambda/8$, the simple estimate predicts a contrast that always exceeds $C > 80\%$.

The width is determined by beam spread and velocity spread. Their influence is easily understood in terms of the transfer function approach of Fig. 4: beam spread causes x_{foc} to be shifted from the perfectly orthogonal case, i.e. ‘atomic beam’ \perp ‘light mask’ (Fig. 4c); velocity spread bends x_{foc} in the focussing region away from the horizontal slope corresponding to infinitely sharp focussing (Fig. 4d). The focussed region is obviously broadened while the defocussed, or pedestal, fraction experiences little deformation. Thus a very simple picture arises: roughly half (in 1D, 1/4 in 2D) of the atoms are focussed while the other half (3/4 in 2D) forms a pedestal. The width of the focussed feature is limited by beam spread and velocity spread, and, furthermore, by diffusive processes such as spontaneous emission and surface migration, which we have omitted here.

In the following two sections, we describe the construction of light masks. The atomic pattern is assumed to closely resemble the light intensity distribution.

3 Complex light masks

Any light mask is generated from the interference of two or more laser beams of a single wavelength. For simplicity we disregard any influence of light polarization on the interference field, so the intensity distribution $I(\mathbf{x}) = I(x, y)$ is inferred from a superposition of electromagnetic waves

$$I(\mathbf{x}) = I_0 \left| \sum_j c_j e^{-i\omega t} e^{i(\mathbf{k}_j \cdot \mathbf{x})} \right|^2, \quad (2)$$

where $I_0 \equiv c \varepsilon_0 |E_0|^2/2$, with c being the speed of light. The coefficients c_j are complex, with $\sum_j |c_j|^2 = 1$. As a rule of thumb each laser beam with another wave vector \mathbf{k}_j contributes a new degree of freedom to the pattern formed by the light field. In this work, however, we introduce a constraint using only \mathbf{k} -vectors that have identical lengths and are restricted to a single plane.

With relatively few laser beams the pattern and its symmetries remain simple and are easily recognized. For instance, an orthogonal arrangement of two counter propagating pairs of laser beams creates a square array of dots [6], and a 120° configuration of three laser beams causes a honeycomb-type structure with six-fold symmetry [7].

More complicated structures will, in general, require more generating laser beams for the construction of the light field.

Using exposure schedules, as they are known from holographic data storage applications, it is no problem to tailor the strength of the grating for each individual beam separately [14]. By application of beam-coupling with an active feed-back loop the phase positions of the gratings can also be controlled [15].

If the required light beams are already known, many (up to 5000) closely spaced individual laser beams can be provided by multiplexed volume holograms (or an alternative diffractive object) with interferometric precision (see [16]). The successful preparation and application of holograms for atomic nanofabrication is described in detail in Sects. 5 and 6. However, how complex the structures to be generated with light masks may be and what types of structures can be generated remains an open question. In (2) it is straightforward to predict the intensity pattern from the electromagnetic waves known and properly arranged in an experiment. The solution to the so-called inverse problem, for which the task is to establish for a known and desired pattern $I(\mathbf{x})$ a configuration of electromagnetic waves that reproduces $I(\mathbf{x})$, or at least gives an approximation $\tilde{I}(\mathbf{x})$ to the interference pattern $I(\mathbf{x})$,

$$\tilde{I}(\mathbf{x}) = I_0 \left| \sum_{j=1}^N \tilde{c}_j e^{-i\omega t} e^{i(\tilde{\mathbf{k}}_j \cdot \mathbf{x})} \right|^2 \approx I(\mathbf{x}) \quad (3)$$

is not known in general. In fact, finding for a given $I(\mathbf{x})$ both the directions $\tilde{\mathbf{k}}_j$ and the normalized partial waves \tilde{c}_j , in addition to the optimal number N , is from a mathematical point of view a highly nonlinear and difficult problem. In approximation theory, the question of how well such objects can be approximated at all in terms of (special cases of) so-called ridge functions $e^{i(\mathbf{k}_j \cdot \mathbf{x})}$ is largely unanswered (see e.g. [17]). In addition, constructive approaches for finding the optimal configuration do not yet exist. Investigations in this direction and numerical results for the inverse problem for a special case have been given for the first time in [18].

Since the pattern is delivered in terms of individual beams with wave vectors \mathbf{k}_j , it is natural to investigate the pattern formed in \mathbf{k} -space. The pattern is in general composed from all possible difference vectors

$$\mathbf{k}_{j,l} \equiv \mathbf{k}_j - \mathbf{k}_l.$$

Periodic structures must show translational invariance and point symmetry. Such crystallographic aspects of interfering light fields have also been investigated in the related subject of optical lattices [19] and have also been extended to quasi-periodic structures [20].

Clearly the maximum vector that can be achieved is $2\mathbf{k}$, corresponding to two exactly counterpropagating waves. All vectors within a circle of radius $2|\mathbf{k}|$ can be realized, but each additional laser beam generates new difference vectors $\mathbf{k}_{j,l}$ with all other waves, hence making a formal analysis difficult. A simpler situation occurs if one beam is much stronger than all others. For simplicity we set $c_1 \equiv 1 \gg |c_j|$, $j \geq 2$, neglecting the small error introduced into the normalization condition used for (2). Since only the difference vectors with this beam will then contribute efficiently to pattern formation, mutual interference of the weaker beams will establish a small

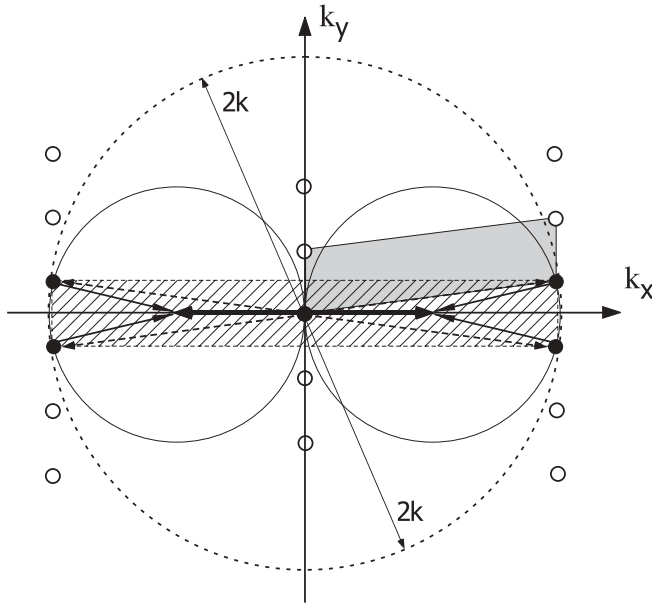


FIGURE 6 Light mask pattern generation in reciprocal space: The simple scheme corresponding to [10]. *Black full dots* mark $k_{j,l}$ -vectors contributing to the pattern of the light field, and *open dots* their periodic extension. The *shaded area* shows the primitive vectors of the Brillouin zone, which is 2D-rhomboidal in this case. 4-fold symmetries of the structure in Fig. 1 are more easily identified with the hatched cell. *Full arrows*, k -vectors of the read-out beam (*thick*) and diffracted beams (*thin*); *dashed arrows*, difference vectors; *full circle*, location of reciprocal vectors for weak interference field; *dashed circle*, maximum range of possible k -vector differences for a given wavelength

and negligible fixed noise pattern. This situation is illustrated for the example from Fig. 1 in Fig. 6.

In general we have for the weak modulation case with one strong read-out and $(N - 1)$ weak diffracted beams

$$\begin{aligned}
 I(\mathbf{x}) &= I_0 \left| e^{-i\omega t} e^{i(\mathbf{k}\cdot\mathbf{x})} + \sum_{j=2}^N c_j e^{-i\omega t} e^{i(\mathbf{k}_j\cdot\mathbf{x})} \right|^2 \\
 &= I_0 \left[1 + 2 \operatorname{Re} \left(\sum_{j=2}^N c_j^* e^{i(\mathbf{k}-\mathbf{k}_j)\cdot\mathbf{x}} \right) \right. \\
 &\quad \left. + \mathcal{O} \left(\sum_{j,l>1} c_j c_l^* \right) \right], \quad (4)
 \end{aligned}$$

which much resembles a conventional Fourier expansion. Wave vectors are in this case, however, restricted to the black full dots in Fig. 6, and the usual Fourier transform can still not be applied.

The k -space picture helps to straightforwardly understand the pattern originating from one strong and two weak waves. However, the primitive vectors of the Brillouin zone form a 2D-rhomboidal structure, while the four-fold symmetry apparent in Fig. 1 is more easily identified also in reciprocal space.

4 Numerical simulations for light mask patterns

As outlined above, for a given intensity pattern, the mathematical determination of the required interfering light

fields is a difficult task. In contrast to omnipresent optical image formation normal to the propagation of light fields, we are concerned here with pattern formation in the plane of propagation. In [18] a method for numerical backward simulation to compute coefficients for arbitrary laser beam configurations to reproduce a specific target image $I(\mathbf{x})$ has been described. In this section, we concentrate on a special case for the inverse problem (see (3)). The number N of laser beams and the wave vectors k_j are fixed a priori.

We will then try to match the target pattern in reciprocal space, not real space. In addition, the difference vectors $k_{j,l}$ are chosen in a particular way. The specific inverse problem is then to determine for a given intensity distribution $I(\mathbf{x})$ the normalized partial waves c_j , $j = 1, \dots, N$, such that the physical pattern \tilde{I} generated as in (3) is ‘close’ to I (in a sense to be discussed). In the method described here we concentrate on a quadratic region in 2D.

The first step is to cover this region by a Cartesian grid and to apply the discrete Fourier transform to I with a certain resolution h . This produces a grid of equal resolution in reciprocal space. To recover the target pattern I , the most relevant points on this grid need to be hit by at least one difference vector $k_{j,l}$. The easiest way is to choose the wave vectors k_j such that the difference vectors $k_{j,l}$ lie on \mathbb{Z}^2 . A prototypic setup is shown in Fig. 7 with $N = 8$ beams.

In this case, these eight beams produce 32 different non-zero difference vectors $k_{j,l}$. Due to this choice of wave vectors, all other Fourier coefficients of the target pattern cannot be reached. Note that the restriction to these particular $k_{j,l}$ introduces an error for general patterns. As most of the differences are located near the origin, the method contains an implicit low-pass filter. This is caused by the setup itself. Different beam configurations will yield different filters, and it may be worthwhile to examine this for a variety of configurations. Here we will restrict ourselves to the setup described above, which is amenable to experimental realization.

The optimal result would be achieved if the coefficients of all 32 difference vectors could be set to the corresponding values of the Fourier transform. This pattern will be denoted \tilde{I}_{opt} . However, we have only $N = 8$ complex degrees of free-

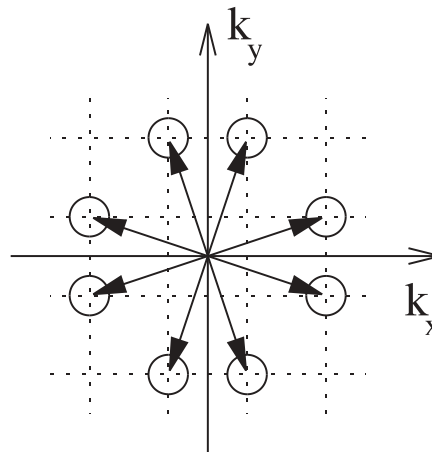


FIGURE 7 A configuration with $N = 8$ beams. The difference vectors $k_{j,l}$ end on integer grid points in reciprocal space (For clarity, only odd grid lines are drawn.)

dom in this example. By expanding the sum in (2) and applying the discrete Fourier transform, we obtain

$$\hat{I}(\mathbf{k}) = \sum_{j,l=1}^8 c_j c_l^* \delta_{\mathbf{k}, \mathbf{k}_{j,l}}. \quad (5)$$

Here \hat{I} denotes the discrete two-dimensional Fourier transform of I after a division by I_0 . All \mathbf{k} -vectors are now in \mathbb{Z}^2 , and the Fourier transform is built up from Kronecker δ -symbols that encode the beam differences $\mathbf{k}_{j,l}$.

We can now treat each of the components in (5) separately. Considering that more than one combination of two beams $\mathbf{k}_j, \mathbf{k}_l$ may produce the same difference vector, we arrive at the following coupled system of nonlinear equations with the complex-valued unknowns $c_j, j = 1, \dots, N$:

$$\hat{I}(\mathbf{0}) = \sum_{j=1}^N |c_j|^2 = 1, \quad (6a)$$

$$\hat{I}(2\mathbf{k}_j) = c_j c_{j+\frac{N}{2}}^* \quad \text{for } j = 1, \dots, \frac{N}{2}, \quad (6b)$$

$$\hat{I}(\mathbf{k}_j - \mathbf{k}_{j+l}) = c_j c_{j+l}^* + c_{j+l+\frac{N}{2}} c_{j+\frac{N}{2}}^* \quad (6c)$$

for $j = 1, \dots, \frac{N}{2}, l = 1, \dots, \frac{N}{2} - 1$.

This is an extension to [18] and holds for any symmetric configuration with an even number of pair-wise different beams. The indices are implicitly wrapped around to fit into the range $1, \dots, N$. Note that this set of equations is complete, as $\hat{I}(-\mathbf{k})$ is the complex conjugate of $\hat{I}(\mathbf{k})$.

In the present setting, we neglect (6a) as it does not contain information about the structure of the pattern. Instead, we build a quadratic least squares minimization functional $J(c_1, \dots, c_N)$ based on (6b) and (6c):

$$J(c_1, \dots, c_N) = \sum_{j=1}^{N/2} \left(\left| \hat{I}(2\mathbf{k}_j) - c_j c_{j+\frac{N}{2}}^* \right|^2 + \sum_{l=1}^{N/2-1} \left| \hat{I}(\mathbf{k}_j - \mathbf{k}_{j+l}) - c_j c_{j+l}^* - c_{j+l+\frac{N}{2}} c_{j+\frac{N}{2}}^* \right|^2 \right). \quad (7)$$

Numerically this is solved by applying a coordinate descent method (see e.g. [21]) that has been adapted to the complex-valued case [18]. In the first step c_2, \dots, c_N are held fixed and $J(c_1, \dots, c_N)$ is minimized exactly with respect to c_1 . Then the minimum is computed with respect to c_2 , and so on. This strategy converges fast up to saturation with a few iterations for $N = 8$.

As the underlying problem is invariant under simultaneous rotation of all coefficients c_j in the complex plane, we expect the numerical solution for different initial values to exhibit this symmetry. This can indeed be observed (see Fig. 8).

Computed reconstructions of images containing the letters 'N' and 'S' are shown in Figs. 9 and 10, respectively. We see that the setup of eight laser beams is already capable of reproducing the significant features of the images. The low-pass effect is clearly visible. Note also that by the nature of the method, the images obey periodic boundary conditions.

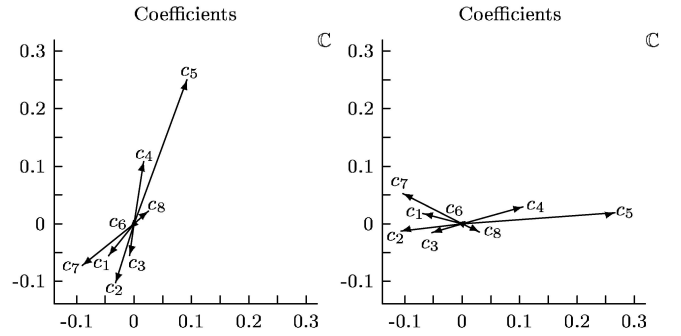


FIGURE 8 The computed coefficients c_j for different choices of initial values. The coefficients are identical up to a rotation



FIGURE 9 Example for $N = 8$, letter 'N'. Left, original pattern I ; Middle, \tilde{I}_{opt} ; Right, reconstructed \tilde{I} by applying the coordinate descent method



FIGURE 10 Example for $N = 8$, letter 'S'. Left, original pattern I ; Middle, \tilde{I}_{opt} ; Right, reconstructed \tilde{I} by applying the coordinate descent method

5 Fabrication of a holographic element for atomic beam lithography

A central aspect of ANF is the use of light masks generating the complex pattern to be transferred to a substrate. Here we describe the use of a photorefractive crystal that diffracts one or more light beams to generate a desired light pattern.

5.1 Recording of the holograms

We use iron-doped photorefractive lithium niobate for recording and multiplexing of elementary volume holographic gratings (LiNbO₃:Fe). Lithium niobate crystals are well known as holographic storage media [22, 23]. Iron appears in LiNbO₃ only in two different valence states Fe²⁺ and Fe³⁺ [24], where the Fe²⁺ ions serve as electron sources and the Fe³⁺ ions as electron traps. Inhomogeneous light excites electrons from Fe²⁺ to the conduction band. The free electrons are redistributed due to drift, diffusion, and the bulk-photovoltaic effect [25]. Finally, they are trapped again at Fe³⁺ ions, which act as empty charge carrier traps, and hence space-charge fields build up and modulate the refractive index of the material via the electro-optical effect.

In our experiments we use a LiNbO₃:Fe crystal with a total iron content of $18 \times 10^{18} \text{ cm}^{-3}$ and a Fe²⁺/Fe³⁺ concentration ratio of 0.1. The dimensions of the sample are $5 \times 5 \times 5 \text{ mm}^3$. To suppress effects arising from Fresnel reflectivity at the surfaces, the two crystal faces perpendicular to the opti-

cal c axis are anti-reflection coated by means of an evaporated MgF_2 film with thickness 145 nm.

We use s -polarized light of a cw-Ti:Sapphire laser (wavelength about 852 nm), which is slightly expanded and spatially filtered ($1/e^2$ -diameter about 4 mm with a Gaussian-shaped intensity profile). Two beam-splitter cubes divide the light into three beams, which are directed onto the crystal by mirrors. Beam I enters the crystal from the front perpendicular to the surface; beams II and III illuminate it from the rear surface symmetrically with an angle $\Theta = 1^\circ$ between each beam and the surface normal (see Fig. 11, left part). The intensity of the three beams is adjusted by combinations of half-wave plates, polarizers, and polarizing beam splitters. All beams have almost equal intensity of 6.2 W/cm^2 (beam I), 5.9 W/cm^2 (beam II), and 7.4 W/cm^2 (beam III). The c -axis is parallel to beam I. Thus the beams I and II record a holographic grating as well as the beams I and III. Although there is interference of the beams II and III, this combination does not significantly contribute to charge carrier redistribution, because the hologram would be perpendicular to the c -axis: In this configuration, no charge driving bulk-photovoltaic effect is present [26, 27] and the diffusion current is very small.

To avoid erasure of the recorded holograms during reading, we apply the technique of thermal fixing [28, 29]. The crystal is heated to 180°C during the recording process. At this elevated temperature, protons become mobile and compensate for the space-charge field of the electronic charge redistribution [30]. After recording, the crystal is cooled down to room temperature. Homogeneous illumination now yields a development of the holograms that are now stable against any readout light.

The Bragg condition that has to be fulfilled for reconstruction of a volume-phase hologram is very pronounced [31, 32]; that is, only reading light of the correct wavelength will reconstruct the signal wave. In our case, the readout wavelength is

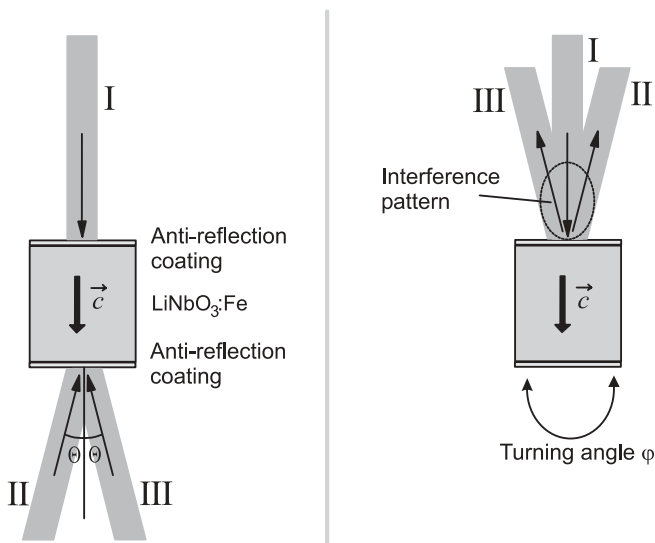


FIGURE 11 Concept of volume holograms stored in a crystal. During the writing process (*left*), the crystal is illuminated with the light beams I, II, and III. For readout (*right*), the crystal is illuminated with beam I, only. The beams II and III are reconstructed simultaneously. Directly in front of the entrance surface, all three beams are present and thus an interference pattern composed of all three beams appears

given by the cesium resonance at which we want to use the volume holograms stored in a crystal; thus the holograms have to be tailored for this requirement. A wavelength accuracy of 0.02 nm is needed to warrant a sufficient diffraction efficiency of the hologram. Using thermal fixing leads to a problem: the thermal expansion of the crystal and its shrinking during cooling down after the writing process changes the Bragg wavelength. To compensate for this effect, we have to increase the recording wavelength by $\Delta\lambda = 0.58 \text{ nm}$ with respect to our desired reading wavelength $\lambda_{\text{read}} = 852.11 \text{ nm}$. First we calibrate the Ti:Sapphire laser to the D_2 line using a spectroscopy cell filled with cesium gas. After that we increase the wavelength by $\Delta\lambda$ and start the hologram recording. The writing time is 2 h because the photorefractive effect is relatively small at near-infrared wavelengths. For shorter wavelengths much shorter writing times of the order of minutes can be expected. To maintain the stability of the interference pattern within the crystal, an active stabilization system is employed that uses beam-coupling effects to derive an error signal in the case of mechanical vibrations of the setup [15, 33, 34]. A piezoelectrically supported mirror in the reference beam can be shifted to realign the correct position of the interference pattern and to suppress the error signal.

5.2 Properties of the holographic element

Two elementary holograms, that is, holographic gratings, are multiplexed. The crystal is illuminated with the reference beam I, and due to diffraction from the two gratings, the beams II and III appear. The diffraction efficiency η of each elementary hologram is defined as the ratio between the diffracted power of beam II or beam III and the incoming power of beam I. This characterization is done at room temperature. We measure η for various turning angles φ of the crystal surface with respect to beam I. The result is shown in Fig. 12 for both reconstructed beams, II and III. Two main results are remarkable:

(A) For perpendicular incidence of beam I, both beams II and III are reconstructed with $\eta \approx 13\%$. If these two diffracted beams interfere with the incident beam I, we obtain an in-

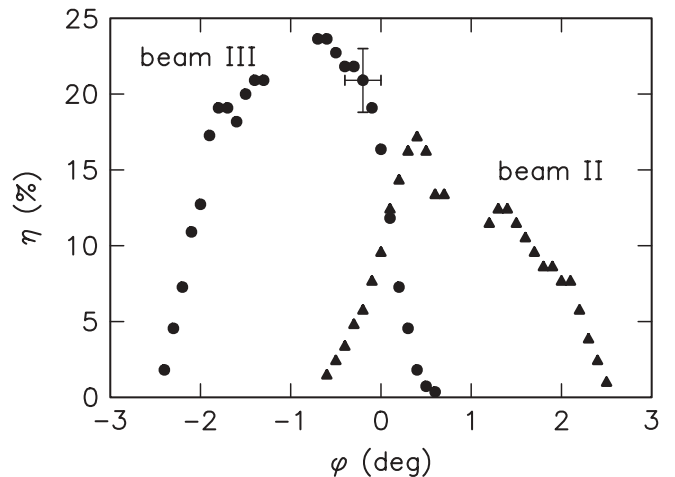


FIGURE 12 Diffraction efficiency η versus angle φ between the crystal surface and readout beam I, plotted for both beams II and III

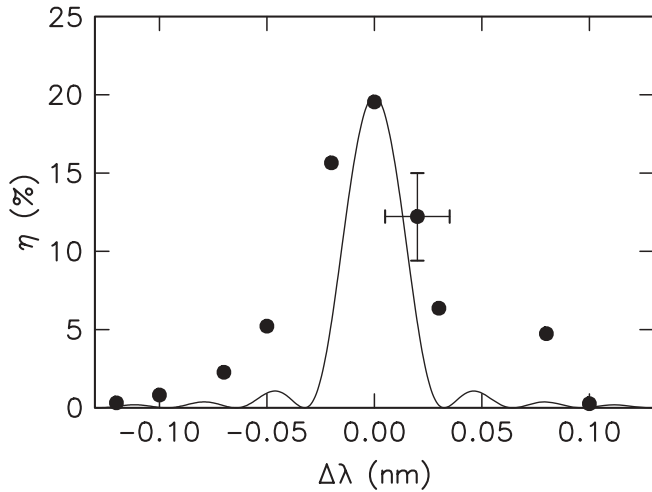


FIGURE 13 Diffraction efficiency η versus detuning of the readout wavelength $\Delta\lambda_{\text{read}}$ for beam III. The markers show measured data; the solid line indicates a calculated curve

terference pattern directly in front of the crystal surface (Fig. 11, right part). The pattern that we expect can be calculated; the result is shown in Figs. 15a and 16a. We get a deeply modulated light pattern with two different period lengths of about 426 nm and 24 μm .

- (B) The angular selectivity of the holographic gratings is checked by varying the angle φ . The diffraction efficiency η versus angle φ is plotted in Fig. 12 for both beams II and III. Figure 12 shows that the maximum values of η do not appear at $\varphi = 0$. It is necessary to change the angle to obtain the optimum values for η for the two beams. Thus the grating period length is slightly too small. Increasing the temperature increases the grating periods and can be utilized to shift the two peaks closer together, but as Fig. 15a shows, the achieved η at $\varphi = 0$ is already sufficient for providing a well-modulated light pattern. Heating the crystal to 35 $^{\circ}\text{C}$ shifts the two maxima together because of thermal expansion of the crystal.

Finally, we vary the reading wavelength λ_{read} by $\Delta\lambda_{\text{read}}$ and check the diffraction efficiency η . The result is shown in Fig. 13: The diffraction efficiency η of beam III is plotted versus changes of the reading wavelength $\Delta\lambda_{\text{read}}$. A mismatch of 0.1 nm already yields a significantly decreased η . The theoretical dependence $\eta(\Delta\lambda_{\text{read}})$ is additionally shown as the solid line in Fig. 13. However, this curve is calculated for a perfect reflection hologram, and it is reasonable that our data do not perfectly match the theoretical expectations. Non-perfect crystal-surface polishing may be a reason for this.

6 Atomic beam lithography experiments

In this chapter we describe our experimental realization of the generation of 2D nanostructures with a light mask generated by multiplexed volume holograms stored in a crystal as discussed in Sect. 5. For this purpose we use an optically collimated, thermal cesium atomic beam.

The atomic beam is produced by thermal evaporation from a cesium oven at about 140 $^{\circ}\text{C}$ (see Fig. 14), leading to a thermal longitudinal velocity distribution with an average atomic speed of roughly 270 m/s. An arrangement of apertures lim-

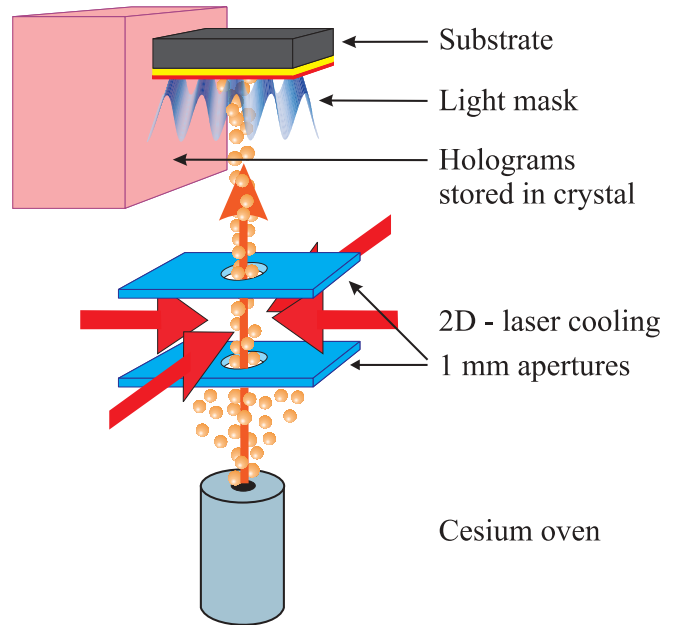


FIGURE 14 Experimental setup for atomic nanofabrication with a holographic mirror. The thermal cesium atomic beam is generated by thermal evaporation. The 2-dimensional laser cooling reduces the transverse velocity. The apertures limit the atomic beam to a diameter of 1 mm and direct it 1 mm off the volume holograms stored in a crystal before the atoms pass the light mask and cling to the substrate

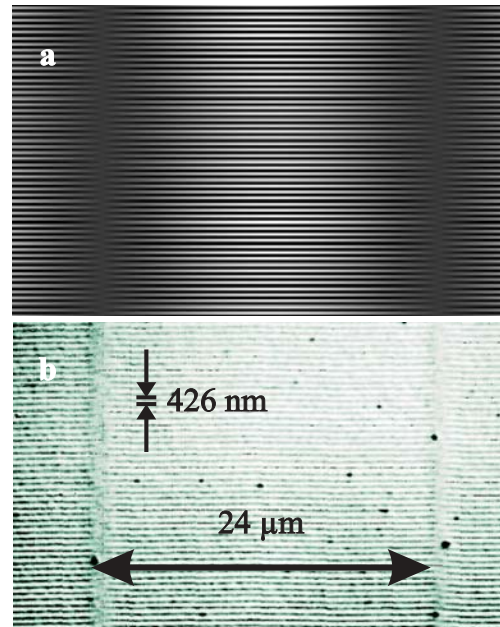


FIGURE 15 **a** Numerical forward simulation of the light mask intensity distribution. **b** Optical microscope picture of gold structures (bright regions) after processing

its the diameter of the atomic beam to 1 mm. The atomic flux density is $5 \times 10^{12} \text{ s}^{-1} \text{ cm}^{-2}$, corresponding to a deposition rate of about one monolayer cesium per 90 s. The transverse velocity of the atomic beam is reduced by 2-dimensional sub-Doppler laser cooling to a remaining divergence of less than 1 mrad.

The holographic element stored in a crystal generating the light mask is mounted above the cooling region. During the

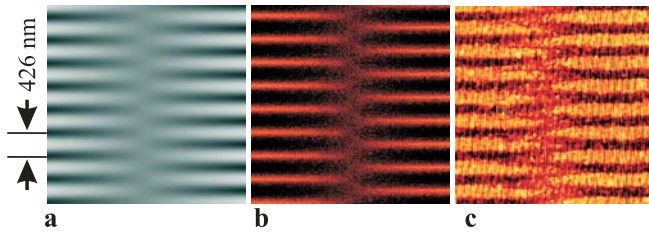


FIGURE 16 **a** Numerical forward simulation of the light mask intensity distribution. **b** Numerical simulation of the atomic flux density in the substrate plane. *Bright regions* indicate a high atomic flux density. **c** Atomic force microscope picture of generated gold structures (*bright regions*)

passage of the cesium atoms through the light mask, optical dipole forces (see (1)) modify the atomic trajectories, resulting in a transverse intensity modulation of the atomic beam behind the light mask.

The volume holograms stored in a crystal are heated up to 35 °C, which was empirically found to give the maximum diffraction efficiency for both stored holographic gratings. The readout laser beam, which propagates from the right side in Fig. 14, has a power of 18 mW and a positive detuning $\Delta = 2\pi$ 600 MHz from the cesium D_2 line at 852 nm. The readout beam is diffracted into two laser beams with a power of 18 and 20%, respectively, relative to the power of the incoming beam. A maximum light mask intensity of 3.5 times the intensity of the readout beam can be calculated from constructive interference of the three contributing laser beams. Destructive interference between the readout beam and the two other beams leads to a minimum intensity of 1.6% of the readout beam intensity. Thus the maximum contrast of the light mask exceeds 99%. As we know from (1), only the derivative of the light mask intensity distribution affects the dipole forces. So even a worse contrast in the light mask can deliver good patterning of the atomic beam. The profiles of all contributing laser beams are Gaussian, with a diameter of $2w_z \approx 170 \mu\text{m}$ in the direction of the atomic beam, and a diameter of $2w_\perp \approx 1.6 \text{ mm}$ transverse to the atomic beam. Hence the atomic beam (diameter 1 mm) is fully covered by all contributing laser beams (see Fig. 14).

The three-beam light mask is slightly modulated by an additional laser beam ($\approx 3\%$), which arises from an additional reflection hologram that is written by back reflection of recording beam I at the rear crystal surface (see Fig. 11a).

During exposure, the substrate is positioned just above the light mask. Best results were achieved when the substrate cut the light mask roughly at the upper beam waist, but good results were even achieved when the substrate position varied about $\pm 50 \mu\text{m}$ in the direction of the atomic beam.

In our case permanent structures are created with highly reactive cesium atoms by applying a resist technique [35, 36]:

The cesium atoms are deposited on a substrate consisting of bulk Si with a 30-nm gold layer, which is covered by a self-assembled monolayer of nonanthirole. This monolayer protects the underlying gold surface from the aqueous gold etching solution. If the cesium dose exceeds a threshold of approximately one monolayer, the resist is destroyed locally. So afterwards the underlying gold can be removed by a dilute etching solution. Therefore this kind of atomic nanofabrication is also called atom lithography.

Figure 15b shows a $35 \mu\text{m} \times 22 \mu\text{m}$ window of a substrate generated by atom lithography with a holographically produced light mask. Dark areas in this high-aperture optical microscope picture indicate substrate regions, where the gold was removed by wet etching, that is, the resist was destroyed by the deposited cesium. The generated pattern is according to the calculated light mask intensity distribution shown in Fig. 15a.

The 2D structure can be divided into two sub-structures:

- (1) Horizontal lines with a spacing of roughly $\lambda/2 = 426 \text{ nm}$, resulting from interference of the readout beam I and the two diffracted beams II and III (see Fig. 11).
- (2) Vertical breaks of the horizontal lines, which repeat at distances of roughly $24 \mu\text{m}$. In Fig. 15 these breaks appear as vertical bands superposing the horizontal lines. These breaks result from destructive interference of beam II and III. Interference of only three beams would result in a constant spacing of $24 \mu\text{m}$ between the breaks. But this spacing is slightly modulated by the weak fourth laser beam mentioned above. The observable dark dots in Fig. 15 are dust particles.

The atomic force microscope picture in Fig. 16c shows a $3.6 \mu\text{m} \times 3.6 \mu\text{m}$ close-up of the generated nano-structures. Bright areas indicate the remaining gold structures after the etching process. This more detailed view reveals that the break of the horizontal lines is combined with a $\lambda/4 = 213 \text{ nm}$ displacement of these lines in the vertical direction, according to our expectations obtained from calculations of the multiple-beam light mask (see (2)).

For comparison of our light mask geometry with the generated results, numerical atomic trajectory simulations were carried out. For this purpose the optical dipole force acting on the atoms passing through the light mask was calculated classically, taking into account our experimental parameters. Figure 16b shows the atomic flux density distribution behind the light mask (see Fig. 16a) in the substrate plane, obtained from calculation of 10^7 atomic trajectories, which represent the position and velocity distribution of our atomic beam. Bright areas represent a high atomic flux density, where the threshold for resist destruction is exceeded and the gold is removed subsequently in the etching process. Hence it is evident that the generated structure (Fig. 16c) is identified as a negative of Fig. 16b. So our experimental results are in very good agreement with our theoretical expectations.

7

Conclusions and outlook

Experimental demonstrations have shown that ANF is a reliable and robust method for producing 1 : 1 structures of any given light mask used here and elsewhere. Generation of more complex light masks with interesting structures is hence an important issue in advancing this method.

In this work we have analyzed the generation of complex light fields by means of multiplexed volume holograms. While we have used a simplified light mask, it has been shown in [16] that up to 5000 holograms can be multiplexed in iron-doped LiNbO_3 . Thus with this method, enormously complex light masks can be generated.

It is an interesting and practically relevant problem to find solutions for the inverse problem of designing a set of light

beams, and hence a holographic element, generating a target pattern. We have carried out initial numerical simulations for this inverse problem by selecting a subset of waves. Our results demonstrate that it is possible to find reasonable approximations for pre-selected wave vectors. It should be emphasized that in order to support sufficient reconstruction quality of specific images an appropriate “conditioning” of the target image is advantageous.

Extensions of the hologram method are straightforward, for example, due to their outstanding angular and wavelength selectivity: (A) by multiplexing holograms with two different read-out waves that have the same wavelength, one may rapidly switch between two different light masks simply by rotating the crystal; and (B) by storing two sets of holograms at different wavelengths, it is possible to manipulate two species of atoms with the same setup and with different patterns.

ACKNOWLEDGEMENTS The authors acknowledge the contributions of M. Flaspöhler, D. Haubrich, and S. Tandler to this work. This work was supported by the Deutsche Forschungsgemeinschaft, the Deutsche Telekom AG, and the European Community. We furthermore thank V. Leung for the careful reading of the manuscript.

REFERENCES

- 1 H. Metcalf, P. van der Straten: *Laser Cooling and Trapping* (Springer, Heidelberg New York 1999)
- 2 C.S. Adams, M. Sigel, J. Mlynek: Phys. Rep. **240**, 143 (1994)
- 3 D. Meschede, H. Metcalf: J. Phys. D: Appl. Phys. **36**, R17 (2003)
- 4 G. Timp, R.E. Behringer, D.M. Tennant, J.E. Cunningham, M. Prentiss, K.K. Berggren: Phys. Rev. Lett. **69**, 1636 (1992)
- 5 J.J. McClelland, R.E. Scholten, E.C. Palm, R. Celotta: Science **262**, 87 (1993)
- 6 R. Gupta, J.J. McClelland, Z.J. Jabbour, R. Celotta: Appl. Phys. Lett. **67**, 1378 (1995)
- 7 U. Drodofsky, J. Stuhler, T. Schulze, M. Drewsen, B. Brezger, T. Pfau, J. Mlynek: Appl. Phys. B **65**, 755 (1997)
- 8 F. Shimizu, J. Fujita: Phys. Rev. Lett. **88**, 123 201 (2002)
- 9 J. Fujita, S. Mitake, F. Shimizu: Phys. Rev. Lett. **84**, 4027 (2000)
- 10 M. Mützel, S. Tandler, D. Haubrich, D. Meschede, K. Peithmann, M. Flaspöhler, K. Buse: Phys. Rev. Lett. **083601-1-4** (2002)
- 11 J.J. McClelland: J. Opt. Soc. Am. B **12**, 1761 (1995)
- 12 K.K. Berggren, M. Prentiss, G. Timp, R.E. Behringer: J. Opt. Soc. Am. B **11**, 1166 (1994)
- 13 W.R. Anderson, C.C. Bradley, J.J. McClelland, R.J. Celotta: Phys. Rev. A **59**, 2476 (1999)
- 14 D. Psaltis, D. Brady, K. Wagner: Appl. Opt. **27**, 1752 (1988)
- 15 P.A.M. Dos Santos, L. Cescato, J. Frejlich: Opt. Lett. **13**, 1014 (1988)
- 16 F.H. Mok: Opt. Lett. **18**, 915 (1993)
- 17 A. Pinkus: Approximating by Ridge Functions. In: *Surface Fitting and Multiresolution Methods*, ed. by A. Le Méhauté, C. Rabut, L.L. Schumaker (Vanderbilt University Press, Nashville, Tennessee 1997) pp. 279–292
- 18 C. Burstedde: Computing Light Masks in Neutral Atom Lithography; manuscript, submitted for publication
- 19 K.I. Petsas, A.B. Coates, G. Grynberg: Phys. Rev. A **50**, 5173 (1994)
- 20 L. Guidoni, C. Triché, P. Verkerk, G. Grynberg: Phys. Rev. Lett. **79**, 3363 (1997)
- 21 D.P. Bertsekas: *Nonlinear Programming*, 2nd edn. (Athena Scientific, Belmont, MA 1999)
- 22 A. Ashkin, G.D. Boyd, J.M. Dziedzic, R.G. Smith, A.A. Ballman, J.J. Levinstein, K. Nassau: Appl. Phys. Lett. **9**, 72 (1966)
- 23 F.S. Chen, J.T. LaMacchia, D.B. Fraser: Appl. Phys. Lett. **13**, 223 (1968)
- 24 H. Kurz, E. Krätzig, W. Keune, H. Engelmann, U. Gonser, B. Dischler, A. Räuber: Appl. Phys. **12**, 355 (1977)
- 25 K. Buse: Appl. Phys. B **64**, 273 (1997)
- 26 V.I. Belinicher, V.K. Malinovskii, B.I. Sturman: Sov. Phys.: JETP **46**, 362 (1977)
- 27 V.I. Belinicher, B.I. Sturman: Sov. Phys.: Uspekhy **23**, 199 (1980)
- 28 J.J. Amodei, D.L. Staebler: Appl. Phys. Lett. **18**, 540 (1971)
- 29 J.J. Amodei, W. Phillips, D.L. Staebler: Appl. Opt. **11**, 390 (1972)
- 30 K. Buse, S. Breer, K. Peithmann, S. Kapphan, M. Gao, E. Krätzig: Phys. Rev. B **56**, 1225 (1997)
- 31 H. Kogelnik: Bell Syst. Tech. J. **48**, 2909 (1969)
- 32 J.W. Goodman: *Introduction to Fourier Optics* (McGraw Hill, New York 1996)
- 33 P.M. Garcia, K. Buse, D. Kip, J. Frejlich: Opt. Commun. **117**, 235 (1995)
- 34 S. Breer, K. Buse, K. Peithmann, H. Vogt, E. Krätzig: Rev. Sci. Instrum. **69**, 1591 (1998)
- 35 M. Kreis, F. Lison, D. Haubrich, D. Meschede, S. Nowak, T. Pfau, J. Mlynek: Appl. Phys. B **63**, 649 (1996)
- 36 F. Lison, H.-J. Adams, D. Haubrich, M. Kreis, S. Nowak, D. Meschede: Appl. Phys. B **65**, 419 (1997)